

NASA  
TP  
1799  
c.1

NASA Technical Paper 1799

LOAN COPY: RE  
AFWL TECHNICA  
KIRTLAND AFB,

0067654



TECH LIBRARY KAFB, NM

# Analysis and Simulation of a Magnetic Bearing Suspension System for a Laboratory Model Annular Momentum Control Device

Nelson J. Groom, Charles T. Woolley,  
and Suresh M. Joshi

MARCH 1981

**NASA**



NASA Technical Paper 1799

Analysis and Simulation of a  
Magnetic Bearing Suspension  
System for a Laboratory Model  
Annular Momentum Control Device

Nelson J. Groom and Charles T. Woolley  
*Langley Research Center*  
*Hampton, Virginia*

Suresh M. Joshi  
*Vigyan Research Associates, Inc.*  
*Hampton, Virginia*

**NASA**

National Aeronautics  
and Space Administration

**Scientific and Technical  
Information Branch**

1981

## SUMMARY

A linear analysis and the results of a nonlinear simulation of a magnetic bearing suspension system which uses permanent magnet flux biasing are presented. The magnetic bearing suspension is part of a 4068 N-m-s (3000 lb-ft-sec) laboratory model annular momentum control device (AMCD). Included in the simulation are rigid body rim dynamics, linear and nonlinear axial actuators, linear radial actuators, axial and radial rim warp, and power supply and power driver current limits.

## INTRODUCTION

The basic concept of the annular momentum control device (AMCD) is that of a rotating annular rim suspended by noncontacting magnetic bearings and powered by a noncontacting linear electromagnetic motor. A detailed discussion of the rationale for the AMCD configuration and its potential applications are presented in reference 1. Earth-based energy storage applications of the concept are discussed in references 2 to 4.

In order to investigate any potential problems in implementing the AMCD concept, a laboratory model AMCD was designed and fabricated under contract. This hardware has been delivered and preliminary tests have been performed. The appendix presents a brief description of the laboratory model, including a table of pertinent physical parameters; reference 5 presents a detailed description. Reference 6 presents results of static and low-speed dynamic tests, which include spin motor torque characteristics and spin motor and magnetic bearing drag losses. Reference 6 also briefly discusses permanent magnetic flux biasing and rim warp. This paper presents an analysis of the laboratory model AMCD magnetic bearing suspension system which addresses the subject of permanent magnet flux biasing and rim warp in more detail. A digital computer simulation, which is used in the analysis of the laboratory model, is described in reference 7. Reference 8 presents the development of an analytical model of the laboratory model magnetic bearing actuator.

## SYMBOLS

Values are given in both SI and U.S. Customary Units. The measurements and calculations were made in U.S. Customary Units.

- [A] matrix defined by equation (10)
- $\bar{F}_A$  total axial force acting on AMCD rim produced by axial bearings a, b, and c
- $F_R$  force produced by a given radial bearing

$F_{Ra}, F_{Rb}, F_{Rc}$  forces produced by radial bearings a, b, and c, respectively  
 $F_{RC}$  force command for a given radial bearing  
 $\bar{F}_{R1}, \bar{F}_{R2}$  forces on AMCD rim along axes 1 and 2, respectively  
 $\{F_X\} = \begin{bmatrix} F_{Xa} & F_{Xb} & F_{Xc} \end{bmatrix}^T$   
 $F_{Xa}, F_{Xb}, F_{Xc}$  forces produced by axial bearings a, b, and c, respectively  
 $G_{A1}, G_{A2}$  torques on AMCD rim about axes 1 and 2, respectively  
 $G_{BR}$  radial bearing transfer function  
 $G_F$  forward loop transfer function of axial bearing loop  
 $G_{FR}$  forward loop transfer function of radial bearing loop  
 $g_R$  gap for a given radial bearing  
 $g_{Ra}, g_{Rb}, g_{Rc}$  gaps for radial magnetic bearings a, b, and c, respectively  
 $g_{RaC}, g_{RbC}, g_{RcC}$  gap commands for radial magnetic bearings a, b, and c, respectively  
 $g_{RC}$  gap command for a given radial bearing  
 $\{g_X\} = \begin{bmatrix} g_{Xa} & g_{Xb} & g_{Xc} \end{bmatrix}^T$   
 $g_{Xa}, g_{Xb}, g_{Xc}$  gaps for axial magnetic bearings a, b, and c, respectively  
 $H_{A03}$  angular momentum stored in rim about spin axis  
 $[I]$  identity matrix  
 $I_A$  moment of inertia of rim about transverse axes  
 $I_{A3}$  moment of inertia of rim about spin axis  
 $K_A$  position gain of a given axial bearing control loop  
 $K_B$  equivalent electromagnet gain of a given magnetic bearing  
 $K_m$  equivalent permanent magnet stiffness of a given magnetic bearing  
 $K_R$  rate gain of a given axial bearing control loop  
 $[M]$  matrix defined by equation (23)  
 $m_A$  mass of rim  
 $r_{CA1}, r_{CA2}, r_{CA3}$  rim translations along axes 1, 2, and 3, respectively

$r_{CA1C}, r_{CA2C}, r_{CA3C}$  rim translation commands along axes 1, 2, and 3, respectively  
 $r_m$  mean radius of rim  
 $s$  Laplace variable  
 $[T]$  matrix defined by equation (11)  
 $W_A$  weight of rim  
 $\theta_{A1}, \theta_{A2}$  rim rotations about axes 1 and 2, respectively  
 $\theta_{A1C}, \theta_{A2C}$  rim rotation commands about axes 1 and 2, respectively  
 $\rho$  damping ratio of axial bearing loop with ideal magnetic bearing  
 $\rho_s$  total system damping ratio  
 $\bar{\rho}$  damping ratio of axial bearing loop with permanent magnet flux biasing  
 $\dot{\phi}_s$  spin rate of rim  
 $\omega_d$  damped natural frequency (eq. 38)  
 $\omega_{DH}$  damped natural frequency of system high-frequency poles  
 $\omega_{DL}$  damped natural frequency of system low-frequency poles  
 $\omega_n$  natural frequency of axial bearing loop with ideal magnetic bearing  
 $\bar{\omega}_n$  natural frequency of axial bearing loop with permanent magnet flux biasing

**Matrix notation:**

$[ ]$  rectangular matrix  
 $[ ]^{-1}$  inverse of rectangular matrix  
 $[ ]^T$  transpose of rectangular matrix  
 $\{ \}$  column vector  
 $[ ]$  row vector

Dots over symbols denote derivatives with respect to time.

## EQUATIONS OF MOTION

The equations of motion used in this paper are for a rigid AMCD rim suspended by magnetic bearings attached to a rigid fixed base. They are described in detail in reference 9. The location of the magnetic bearing suspension stations with respect to the AMCD axis system is shown in figure 1.

The axial gaps, in terms of rim rotations and translations, are given by

$$\begin{Bmatrix} g_{Xa} \\ g_{Xb} \\ g_{Xc} \end{Bmatrix} = \begin{bmatrix} (\sqrt{3}/2)r_m & -(1/2)r_m & 1 \\ -(\sqrt{3}/2)r_m & -(1/2)r_m & 1 \\ 0 & r_m & 1 \end{bmatrix} \begin{Bmatrix} \theta_{A1} \\ \theta_{A2} \\ r_{CA3} \end{Bmatrix} \quad (1)$$

where  $g_{Xa}$ ,  $g_{Xb}$ , and  $g_{Xc}$  are the axial gaps for bearing stations a, b, and c, respectively,  $r_m$  is the mean radius of the AMCD rim,  $\theta_{A1}$  and  $\theta_{A2}$  are rotations of the rim about axes 1 and 2, respectively, and  $r_{CA3}$  is the translation of the rim along axis 3. The radial gaps in terms of rim translations are

$$\begin{Bmatrix} g_{Ra} \\ g_{Rb} \\ g_{Rc} \end{Bmatrix} = \begin{bmatrix} 1/2 & \sqrt{3}/2 \\ 1/2 & -\sqrt{3}/2 \\ -1 & 0 \end{bmatrix} \begin{Bmatrix} r_{CA1} \\ r_{CA2} \end{Bmatrix} \quad (2)$$

where  $g_{Ra}$ ,  $g_{Rb}$ , and  $g_{Rc}$  are the radial gaps for bearing stations a, b, and c, respectively, and  $r_{CA1}$  and  $r_{CA2}$  are translations of the AMCD rim along axes 1 and 2, respectively. The torques on the rim due to the axial bearing forces are

$$\begin{Bmatrix} G_{A1} \\ G_{A2} \end{Bmatrix} = \begin{bmatrix} (\sqrt{3}/2)r_m & -(\sqrt{3}/2)r_m & 0 \\ -(1/2)r_m & -(1/2)r_m & r_m \end{bmatrix} \begin{Bmatrix} F_{Xa} \\ F_{Xb} \\ F_{Xc} \end{Bmatrix} \quad (3)$$

where  $G_{A1}$  and  $G_{A2}$  are torques on the rim about axes 1 and 2, respectively, and  $F_{Xa}$ ,  $F_{Xb}$ , and  $F_{Xc}$  are the axial forces produced by bearing stations a, b, and c, respectively. The radial forces resolved along axes 1 and 2 are

$$\begin{Bmatrix} \bar{F}_{R1} \\ \bar{F}_{R2} \end{Bmatrix} = \begin{bmatrix} 1/2 & 1/2 \\ \sqrt{3}/2 & -\sqrt{3}/2 \end{bmatrix} \begin{bmatrix} -1 \\ 0 \end{bmatrix} \begin{Bmatrix} F_{Ra} \\ F_{Rb} \\ F_{Rc} \end{Bmatrix} \quad (4)$$

where  $\bar{F}_{R1}$  and  $\bar{F}_{R2}$  are forces on the rim along axes 1 and 2 and  $F_{Ra}$ ,  $F_{Rb}$ , and  $F_{Rc}$  are the radial forces produced by bearing stations a, b, and c, respectively. The rim rotational and axial translation dynamics are

$$I_A \ddot{\theta}_{A1} = G_{A1} - H_{A03} \dot{\theta}_{A2} \quad (5a)$$

$$I_A \ddot{\theta}_{A2} = G_{A2} + H_{A03} \dot{\theta}_{A1} \quad (5b)$$

$$m_A \ddot{r}_{CA3} = \bar{F}_A - W_A \quad (5c)$$

where  $I_A$  is the rim transverse inertia,  $m_A$  is the rim mass,  $H_{A03}$  is the rim angular momentum about axis 3 (the spin axis), and  $W_A$  is the weight of the rim,

$$\bar{F}_A = F_{Xa} + F_{Xb} + F_{Xc} \quad (6)$$

Finally, the radial translation dynamics become

$$m_A \begin{Bmatrix} \ddot{r}_{CA1} \\ \ddot{r}_{CA2} \end{Bmatrix} = \begin{Bmatrix} \bar{F}_{R1} \\ \bar{F}_{R2} \end{Bmatrix} \quad (7)$$

#### MAGNETIC BEARING SUSPENSION SYSTEM

The laboratory model AMCD magnetic bearing suspension system provides active positioning control of the rim in both the axial and radial directions. The axial and radial suspension systems are independent and are designed separately.

#### Axial System

Assuming three magnetic bearing suspension stations equally spaced around the rim and ideal rim inertia distribution, it will be shown subsequently that axial motions of the rim in each of the bearing stations are uncoupled at zero rim speed. That is, axial motion of the rim in one bearing produces no motion in the other two bearings. Consequently, at zero momentum, the axial magnetic

bearing control system decouples into three identical independent systems. Thus, a single design, using a simplified suspended mass model, can be performed for each system. Applying this decoupled design approach to the laboratory model AMCD, the closed-loop magnetic bearing control system parameters required to produce desired system performance at a given rim angular momentum are obtained by analyses similar to those in reference 1 but with respect to a fixed base.

To illustrate this approach, the axial system characteristic equation will be developed with the assumption that the magnetic bearing actuators are perfect (i.e., force output is equal to force command) and that the force commands are functions of rim position and rate. Under these assumptions, the bearing force  $F$  as a function of bearing gap  $g$  at a given bearing station can be written as

$$F = G_F g = (K_A + K_R s)g \quad (8)$$

where  $K_A$  is a position gain,  $K_R$  is rate gain,  $G_F$  is the forward loop transfer function, and  $s$  the Laplace operator. The rim rotational and axial translation equations of motion are given in equations (5). Taking the Laplace transform of these equations and putting them in matrix form results in

$$\begin{bmatrix} I_A s^2 & H_{A03} s & 0 \\ -H_{A03} s & I_A s^2 & 0 \\ 0 & 0 & m_A s^2 \end{bmatrix} \begin{Bmatrix} \theta_{A1} \\ \theta_{A2} \\ r_{CA3} \end{Bmatrix} = \begin{Bmatrix} G_{A1} \\ G_{A2} \\ \bar{F}_A \end{Bmatrix} \quad (9)$$

In order to simplify the terms in the following development, define

$$[A] = \begin{bmatrix} I_A s^2 & H_{A03} s & 0 \\ -H_{A03} s & I_A s^2 & 0 \\ 0 & 0 & m_A s^2 \end{bmatrix} \quad (10)$$

and

$$[T] = \begin{bmatrix} (\sqrt{3}/2) r_m & -(1/2) r_m & 1 \\ -(\sqrt{3}/2) r_m & -(1/2) r_m & 1 \\ 0 & r_m & 1 \end{bmatrix} \quad (11)$$

Equation (9) becomes

$$[A] \left\{ \frac{\theta_A}{r_{CA3}} \right\} = \left\{ \frac{G_A}{\bar{F}_A} \right\} = [T]^T \{F_X\} \quad (12)$$

The bearing forces are functions of the bearing gap displacements  $\{g_X\}$  and commands  $\{g_{XC}\}$  as given by

$$\{F_X\} = G_F (\{g_{XC}\} - \{g_X\}) \quad (13)$$

where  $G_F$  is defined by equation (8). Converting gaps to angles and displacements by using equation (1) results in

$$[A] \left\{ \frac{\theta_A}{r_{CA3}} \right\} = G_F [T]^T [T] \left( \left\{ \frac{\theta_{AC}}{r_{CA3C}} \right\} - \left\{ \frac{\theta_A}{r_{CA3}} \right\} \right) \quad (14)$$

or

$$([A] + G_F [T]^T [T]) \left\{ \frac{\theta_A}{r_{CA3}} \right\} = G_F [T]^T [T] \left\{ \frac{\theta_{AC}}{r_{CA3C}} \right\} \quad (15)$$

The system characteristic equation becomes

$$\det | [A] + G_F [T]^T [T] | = 0 \quad (16)$$

Expanding the determinant and making appropriate substitutions results in

$$[m_A s^2 + 3(K_{RS} + K_A)] \{ [I_A s^2 + (3/2) r_m^2 (K_{RS} + K_A)]^2 + H_{A03} s^2 \} = 0 \quad (17)$$

Making the thin rim assumption

$$I_A = \frac{m_A r_m^2}{2} \quad (18)$$

and setting  $H_{A03}$  to zero allows equation (17) to be simplified to

$$\left( s^2 + \frac{K_R}{m_A/3} s + \frac{K_A}{m_A/3} \right)^3 = 0 \quad (19)$$

which illustrates the zero-momentum decoupling mentioned earlier. Referring to equation (17), it can be seen that the translational roots are obtained from

$$m_A s^2 + 3(K_R s + K_A) = 0$$

and are unaffected by the system momentum. The natural frequency of a single station becomes

$$\omega_n = \sqrt{\frac{K_A}{m_A/3}}$$

with a damping ratio of

$$\rho = \frac{K_R}{2 \sqrt{K_A (m_A/3)}}$$

In order to examine the effects of momentum, the second product term of equation (17) is expanded to yield

$$s^4 + \frac{3r_m^2 K_R}{I_A} s^3 + \left[ \frac{H_{A03}^2}{I_A^2} + \frac{3r_m^2 K_A}{I_A} + \left( \frac{3}{2} \frac{r_m^2 K_R}{I_A} \right)^2 \right] s^2 + 2 \left( \frac{3}{2} \frac{r_m^2}{I_A} \right)^2 K_R K_A s + \left( \frac{3}{2} \frac{r_m^2 K_A}{I_A} \right)^2 = 0 \quad (20)$$

With the use of equation (18), equation (20) can be expressed in terms of the zero-momentum natural frequency and damping ratio of a single station as follows:

$$s^4 + 4\rho\omega_n s^3 + \left[ \left( \frac{H_A 0.3}{I_A} \right)^2 + 2(1 + 2\rho^2)\omega_n^2 \right] s^2 + 4\rho\omega_n^3 s + \omega_n^4 = 0 \quad (21)$$

Using the parameters of the laboratory model AMCD (described in the appendix) with  $K_A$  set at the laboratory model design goal (ref. 5) of 262.7 N/mm (1500 lb/in.) and assuming rated momentum (4068 N-m-s or 3000 lb-ft-sec), the damping ratio of the dominant system roots can be plotted against the damping ratio of a single bearing station at zero momentum as shown in figure 2. The implication of figure 2 is that if no practical limitations on rate gain exist then acceptable system performance is possible by designing for independent station control.

The roots of equation (21), which represent the system poles, have some interesting characteristics which warrant discussion. At zero momentum there are, of course, two identical sets of poles. As the rim momentum increases, the poles form a set of high-frequency and a set of low-frequency complex poles. One set of poles increases in natural frequency as the rim momentum increases, and the other set decreases in natural frequency. The damping ratio is the same for each set of complex poles. For purposes of illustration, consider a damping ratio  $\rho$  of 1.65 which, from figure 2, should result in  $\rho_s$  of 0.7 at full speed. With this value of  $\rho$  and the same parameters used to generate figure 2, the zero-speed poles of equation (21) become

$$(s + 63.2)^2 (s + 554.9)^2$$

Figure 3 shows the motion of the low-frequency poles in the upper left quadrant of the s-plane as rim speed is varied from 0 to 2700 rpm. Figure 4 is a similar plot for the high-frequency poles. If the poles are complex at zero rim speed, both sets start at the same location in the s-plane and separate as rim speed increases.

#### Radial Design

The radial design problem is somewhat simpler than the axial design since momentum coupling is not involved. One consideration for the radial system, however, is rim growth at high speeds. A method of compensating for this in the laboratory model AMCD is presented in reference 5. As was the case with the axial system, the radial system will only be discussed in general terms.

The equations of motion for the rim in the radial direction are

$$m_A \begin{Bmatrix} \ddot{x}_{CA1} \\ \ddot{x}_{CA2} \end{Bmatrix} = \begin{Bmatrix} \bar{F}_{R1} \\ \bar{F}_{R2} \end{Bmatrix} \quad (22)$$

where  $\bar{F}_{R1}$  and  $\bar{F}_{R2}$  are defined by equation (4). In order to simplify the terms in the following development, define

$$[M] = \begin{bmatrix} 1/2 & \sqrt{3}/2 \\ 1/2 & -\sqrt{3}/2 \\ -1 & 0 \end{bmatrix} \quad (23)$$

The force command for a given radial bearing  $F_{RC}$  can be written as

$$F_{RC} = G_{FR}(g_{RC} - g_R) \quad (24)$$

where  $G_{FR}$  is the forward loop transfer function of the radial loop,  $g_{RC}$  is the radial gap command, and  $g_R$  is the radial gap. The force produced by a given bearing becomes

$$F_R = G_{BR}F_{RC} \quad (25)$$

where  $G_{BR}$  is the radial bearing transfer function. The total bearing forces become

$$\begin{Bmatrix} F_{Ra} \\ F_{Rb} \\ F_{Rc} \end{Bmatrix} = G_{FR}G_{BR} \begin{Bmatrix} g_{RaC} - g_{Ra} \\ g_{RbC} - g_{Rb} \\ g_{RcC} - g_{Rc} \end{Bmatrix} \quad (26)$$

The radial forces along axes 1 and 2 become (from eq. (4))

$$\begin{Bmatrix} \bar{F}_{R1} \\ \bar{F}_{R2} \end{Bmatrix} = G_{FR}G_{BR}[M]^T \begin{Bmatrix} g_{RaC} - g_{Ra} \\ g_{RbC} - g_{Rb} \\ g_{RcC} - g_{Rc} \end{Bmatrix} \quad (27)$$

In terms of rim displacements, equation (27) becomes (from eq. (2))

$$\begin{Bmatrix} \bar{F}_{R1} \\ \bar{F}_{R2} \end{Bmatrix} = G_{FR}G_{BR}[M]^T[M] \begin{Bmatrix} r_{CA1C} - r_{CA1} \\ r_{CA2C} - r_{CA2} \end{Bmatrix} \quad (28)$$

Using equation (22), equation (28) can be written as

$$(m_{AS}^2[I] + G_{FR}G_{BR}[M]^T[M]) \begin{Bmatrix} r_{CA1} \\ r_{CA2} \end{Bmatrix} = G_{FR}G_{BR}[M]^T[M] \begin{Bmatrix} r_{CA1C} \\ r_{CA2C} \end{Bmatrix} \quad (29)$$

where [I] is the identity matrix. The system characteristics equation becomes

$$\det \left| (m_{AS}^2[I] + G_{FR}G_{BR}[M]^T[M]) \right| = 0 \quad (30)$$

Expansion of this determinant results in

$$(m_{AS}^2 + 1.5G_{FR}G_{BR})^2 = 0 \quad (31)$$

If perfect actuators are assumed (i.e.,  $G_{BR} = 1$ ) and if  $G_{FR}$  is a function of position and rate, then the radial system design reduces to that of a second-order spring mass system.

## PRACTICAL CONSIDERATIONS

Initial tests with the laboratory model AMCD have provided insight into limitations of two hardware design approaches taken. These approaches, which are also discussed in reference 6, are (1) completely unidirectional layup of composite materials in the rim and (2) permanent magnet flux biasing for the bearings. Other hardware characteristics that warrant discussion are distributed bearing elements and magnetic bearing power driver and power supply current limits.

### Rim Fabrication

The laboratory model AMCD rim was fabricated by wrapping a graphite filament tape, impregnated with resin, on a special spindle producing 100-percent circumferential fibers (ref. 5). As discussed in reference 6, this makes the rim susceptible to creep in a direction parallel to the spin axis; this results in deviations of the rim out of the spin plane which produces an equivalent disturbance input to the axial bearings as the rim spins. In the laboratory model

AMCD, static deviations of the rim have been measured to be a maximum of 1.651 mm (0.065 in.) to a minimum of 0.2032 mm (0.008 in.) depending on how the rim is stored. These numbers are total deviations (measured from peak to peak) and were measured midway between suspension stations with the rim suspended. The rim deviations, or warp, include two high and two low points per rim revolution which approximate a sine wave disturbance at twice the wheel spin frequency. The origin of the basic two cycle per revolution shape of the warp is unknown. By experimenting with different methods of storing the rim, it was found that rim deviations could be held consistently to within 0.381 mm (0.015 in.) peak to peak.

### Permanent Magnet Flux Biasing

As mentioned earlier, the AMCD laboratory model magnetic bearings utilize permanent magnet flux biasing. Advantages of this technique include: (1) A linear relationship between force and current at a given operating point can be easily obtained; (2) with permanent magnets supplying a portion of the flux, the power required to suspend the rim in a 1g (1g = 9.8 m/s<sup>2</sup> (32.2 ft/sec<sup>2</sup>)) environment is reduced. This technique does, however, present some problems from a control system standpoint. In order to discuss these problems, the linearized mathematical model of the AMCD laboratory model magnetic bearing actuator, derived in reference 9 (eq. (43)), is incorporated into equation (13) to yield

$$\{F_X\} = K_B G_F (\{g_{XC}\} - \{g_X\}) + K_m \{g_X\} \quad (32)$$

where the force command is represented as the current to the electromagnet. Equation (14) then becomes

$$[A] \begin{pmatrix} \theta_A \\ r_{CA3} \end{pmatrix} = K_B G_F [T]^T [T] \left( \begin{pmatrix} \theta_{AC} \\ r_{CA3C} \end{pmatrix} - \begin{pmatrix} \theta_A \\ r_{CA3} \end{pmatrix} \right) + K_m [T]^T [T] \begin{pmatrix} \theta_A \\ r_{CA3} \end{pmatrix} \quad (33)$$

and the system characteristic equation becomes

$$\det \left| [A] + [T]^T [T] (K_B G_F - K_m) \right| = 0 \quad (34)$$

Expanding the determinant and making appropriate substitutions results in

$$\begin{aligned} & \left[ m_A s^2 + 3K_B K_{RS} + 3(K_B K_A - K_m) \right] \left\{ \left[ I_A s^2 + 3/2 r_m^2 K_B K_{RS} \right. \right. \\ & \left. \left. + (3/2) r_m^2 (K_B K_A - K_m) \right]^2 + H_{A03}^2 s^2 \right\} = 0 \end{aligned} \quad (35)$$

Expanding the rotational part results in

$$s^4 + \frac{3r_m^2 K_B K_R s^3}{I_A} + \left[ \frac{H_{A03}^2}{I_A^2} + \frac{3r_m^2 (K_B K_A - K_m)}{I_A} + \left( \frac{3}{2} \frac{r_m^2 K_B K_R}{I_A} \right)^2 \right] s^2 + 2 \left( \frac{3}{2} \frac{r_m^2}{I_A} \right)^2 K_B K_R (K_B K_A - K_m) s + \left[ \frac{3}{2} r_m^2 \frac{(K_B K_A - K_m)}{I_A} \right]^2 = 0 \quad (36)$$

Making the substitutions

$$\bar{\omega}_n = \sqrt{\frac{(K_B K_A - K_m)}{m_A/3}}$$

and

$$\bar{\rho} = \frac{K_B K_R}{2 \sqrt{(K_B K_A - K_m) (m_A/3)}}$$

equation (36) can be put in the following form:

$$s^4 + 4\bar{\rho}\bar{\omega}_n s^3 + \left[ \left( \frac{H_{A03}}{I_A} \right)^2 + 2(1 + 2\bar{\rho}^2)\bar{\omega}_n^2 \right] s^2 + 4\bar{\rho}\bar{\omega}_n^3 s + \bar{\omega}_n^4 = 0 \quad (37)$$

which is the same form as equation (21). As illustrated by figure 2, if no practical limit on rate gain exists, then acceptable system performance at full rim speed can be obtained. In the case of the AMCD laboratory model, an upper limit was imposed by a rim bending mode being driven unstable (ref. 5). The upper limit on rate gain, from reference 5, was calculated to be 66.3 A-s/m (20.2 A-sec/ft) with a position gain of 19571 A/m (5965 A/ft). This results in  $\bar{\rho} = 0.365$  (using the value of  $K_m$  from ref. (9)) and  $\bar{\omega}_n = 157.86$  rad/s. Using the relationship  $H_{A03} = I_{A3}\phi_s$ , the curve of figure 5, which is a plot of the damping ratio of the dominant system poles versus rim speed, can be generated. As mentioned earlier in the discussion of equation (21), equation (37) has two sets of complex poles which are equal at zero rim speed. As the rim spins up, the natural frequency of one set of poles becomes higher than the zero-speed value and for the other set it becomes lower. Figure 6 is a plot of the damped natural frequency of the poles of equation (37) versus the rim

spin speed. The damping ratio of both sets of poles is the same. The damped natural frequency, defined as

$$\omega_d = \omega_n \sqrt{1 - \rho^2} \quad (38)$$

is the frequency contributed to total system response by each set of poles and is the frequency at which the gain peaks for a set of underdamped poles on a magnitude frequency response plot. (For a discussion of frequency response methods and transient analysis by transfer function, see ref. 10.) Note from the figure that the low-frequency, or dominant, poles have a damped natural frequency  $\omega_{DL}$  equal to twice the rim speed at approximately 500 rpm and equal to the rim speed at approximately 830 rpm. The crossover at twice rim speed is significant because the fundamental frequency of the rim warp is at this speed. Because of the increased motion of the rim in the bearing gaps at this resonance point, the linearization of the magnetic bearing actuators is no longer valid. Some insight, from a linear analysis standpoint, into the dynamics of large motions of the rim in the bearing gaps can be gained by referring to figures 7 and 8. These are plots of  $K_B$  and  $K_m$  versus their corresponding operating points in the bearing gaps. With rate and position gains fixed at 66.3 A-s/m (20.2 A-sec/ft) and 19571 A/m (5965 A/ft),  $\bar{\omega}_n$  and  $\bar{\rho}$  vary over the same range of operating points as shown in figures 9 and 10.

#### Distributed Bearing Elements

As described in the appendix, each magnetic bearing station consists of four magnetic elements top and bottom for the axial suspension and four elements mounted around the inside of the rim for the radial suspension. The axial position sensor is mounted in the center of the top four bearing elements, and the radial position sensor is mounted in the center of the radial elements. This means that the bearing forces are being applied at points displaced from the point at which position is sensed. Incorporating the bearing element and sensor positions into equation (32) results in a negligible change in the system characteristic equations. The effects of rim warp and nonlinear bearing characteristics combined with distributed bearing elements produced a dynamic system model which was best investigated using the digital computer simulation described in reference 7.

#### Power Driver and Power Supply Current Limits

The laboratory model AMCD magnetic bearing power drivers (described in ref. 5) have a voltage limit of  $\pm 20$  V. This voltage limit, in conjunction with the bearing coil resistance, results in an equivalent current limit of 13.13 A. In addition, the system power supply has a current limit of 30 A.

## SIMULATION RESULTS AND DISCUSSION

In order to evaluate the effects of rim warp, permanent magnet flux biasing, distributed bearing elements, and power driver and power supply current limits, the digital computer simulation, described in reference 8, was developed. Figure 11 contains plots of peak-to-peak rim motion in a given axial magnetic bearing (peak-to-peak motion was the same in all stations) versus rim spin speed for the full nonlinear model with two rim warp amplitudes. The two amplitudes were 0.9525 mm (0.00375 in.) and 0.1905 mm (0.0075 in.) which produced peak-to-peak static deviations measured midway between suspension stations of 0.381 mm (0.015 in.) and 0.762 mm (0.030 in.), respectively. Figure 11 also contains plots of peak system current for the same rim warp amplitudes versus rim spin speed. For comparison purposes, simulation runs were made using a single point nonlinear axial bearing model and a single point linear axial bearing model, each with power driver and power supply current limits removed. The results are presented in figures 12 and 13.

The main points to be made about these results are: (1) Rim motion is stable through the resonance excited by the rim warp for all cases. (2) The rim speed at which resonance occurs, for all cases, is very close to that predicted by figure 6. (3) The resonance peak, for the rate gain considered, was approximately twice the warp peak amplitude. (4) The amplitudes and shapes of the plots for the single point linear and single point nonlinear bearings were very similar, and these plots showed only slight differences from the plots for the nonlinear distributed case.

All of this tends to lend considerable confidence in subsequent linear analyses using the single point linear bearing model. However, the simulation runs differed from the actual hardware performance in two ways. First, the laboratory model was unable to attain a stable spin speed in excess of 475 rpm. Second, the radial current increase, as the rim was spun up, was much lower in the simulation than in the laboratory model. Recent tests, with a new magnetic bearing system installed in the laboratory model, have identified a static imbalance of the rim in the radial direction. Since the radial rim warp was the only anomaly included in the simulation, it appears likely that the major increase in current, as rim speed was increased in the laboratory model tests, was due to the static imbalance.

In an effort to identify possible mechanisms for dynamic instability, simulation runs were made using the full nonlinear model with increasing values of warp amplitude. The system became unstable at a warp amplitude of 0.3226 mm (0.0127 in.). The speed at which the instability occurred was approximately 770 rpm. The cause of the instability was a reduction in effective gains due to power supply and power driver limits being exceeded. It is interesting to note that the system became dynamically unstable before rim motion became large enough to trigger the backup bearing system.

In order to investigate the effects of zero-speed single station damping ratios on system stability, further runs were made using the warp amplitude of 0.3226 mm (0.0127 in.) but with zero-speed single station damping ratios of 0.2 and 0.7. With a damping ratio of 0.2, the speed at which the system went unstable was reduced to approximately 410 rpm. When the damping ratio was

increased to 0.7, the system was stable over the same range even though the power driver and power supply current limits were exceeded.

To summarize, the results obtained from the simulation were: (1) With rim warp as the only anomaly included in the radial system, no power supply or power driver limits were exceeded for axial rim warp values up to 0.1905 mm (0.0075 in.) peak to peak, and the system exhibited stable operation. Results for distributed nonlinear, single point nonlinear, and single point linear axial actuators were similar. (2) By increasing the value of the axial warp amplitude, a mechanism for dynamic instability for the axial system was identified. This mechanism was the reduction in effective gains due to power supply and power driver limits being exceeded. (3) Dynamic instability occurred before rim motion became large enough to trigger the backup bearing system. (4) Under conditions where dynamic instability was possible, zero-speed single station damping ratio had a significant effect on the speed at which the instability occurred.

#### CONCLUDING REMARKS

A linear analysis and the results of a nonlinear simulation of a magnetic bearing suspension system which uses permanent magnet flux biasing has been presented. The magnetic bearing suspension is part of a 4068 N-m-s (3000 lb-ft-sec) laboratory model AMCD. Included in the simulation were rigid body rim dynamics, linear and nonlinear axial actuators, linear radial actuators, axial and radial rim warp, and power supply and power driver current limits.

The linear analysis of the magnetic bearing suspension system for the laboratory model AMCD indicated that stable system operation can be achieved by utilizing independent single station axial control. The single station bearing control system design can be performed using zero rim speed parameters. System performance at rated rim speed is influenced by the zero-speed single station damping ratio.

The nonlinear simulation indicated that for rim axial warp amplitudes up to 0.1905 mm (0.0075 in.) peak to peak and for system operation where power supply and power driver limits were not exceeded, the linear and nonlinear axial bearing models gave similar results and the system was stable, as predicted by the linear analysis. For this warp amplitude range, however, the simulation runs differed from the actual hardware performance in two ways. First, the laboratory model was unable to attain a stable spin speed in excess of 475 rpm. Second, the radial current increase, as the rim was spun up, was much lower in the simulation than in the laboratory model. Recent tests, with a new magnetic bearing system installed in the laboratory model, have identified a static imbalance of the rim in the radial direction. Since the radial rim warp was the only anomaly included in the simulation, it appears likely that the major increase in radial current, in the laboratory tests, was due to static imbalance.

By increasing the value of the axial rim warp in the simulation, a mechanism for dynamic instability was identified. This mechanism was the reduction in effective axial system gains due to power supply and power driver limits being exceeded. Dynamic instability occurred before rim motion reached a level

that would have triggered the backup bearing system. Under conditions where dynamic instability was possible, zero-speed single station damping ratio was found to have a significant effect on the speed at which instability occurred.

Langley Research Center  
National Aeronautics and Space Administration  
Hampton, VA 23665  
January 22, 1981

## APPENDIX

### LABORATORY MODEL AMCD

This appendix presents a brief description of the laboratory model AMCD assembly. A more detailed description of the subsystems are given in reference 5. The laboratory model, shown in figure A1, consists of a graphite-epoxy composite rim which is 1.6 m (63 in.) in diameter, weighs 22.5 kg (49.5 lb), and is designed to rotate at a speed of 2741 rpm. At this speed the rim momentum is 4068 N-m-s (3000 lb-ft-sec). The rim is suspended by three equally spaced support stations. Magnetic bearing elements located in the support stations interact with a low-loss ferrite material, embedded in the rim, to produce radial and axial suspension forces. Electromagnetic stator elements, also located at the support stations, push and pull against 72 equally spaced samarium cobalt permanent magnets, embedded in outer edge of the rim, to produce spin torques. The stator element drive electronics are commutated by signals from a Hall effect device which senses the position of the magnets.

In order to prevent damage to the rim in the event of a magnetic suspension failure during spin tests, the AMCD laboratory model includes a backup bearing system. The backup system includes six bearings (two per suspension station) which are designed to slow and support the rim. The bearing design provides hydrostatic air pads for radial control and hydrodynamic air pads for axial control. The backup and suspension bearing assemblies are attached to an aluminum baseplate. A vacuum cover (not shown) fits over the bearing-motor-rim assembly and also attaches to the baseplate. The cover is used for high-speed spin tests only.

Figure A2 presents a close-up of one of the suspension stations. There are four magnetic bearing elements, top and bottom, for the axial suspension and four elements mounted around the inside of the rim for the radial suspension. The center structure mounts the axial and radial position sensors for this station. The sensors consist of a variable impedance bridge with an active and a reference coil. They are sensitive to anything that changes the inductance of the active coil in the sensor probe such as the close proximity of a magnetic material. In the AMCD rim the ferrite material is sensed. Figure A3 is a cross-section drawing taken through a bearing station and shows the rim, bearings, and spin motor elements in more detail. The magnetic bearing gaps with the rim centered are 2.54 mm (0.1 in.). Pertinent physical parameters of the laboratory model AMCD are listed in table A1.

APPENDIX

TABLE A1

PHYSICAL PARAMETERS OF LABORATORY MODEL AMCD

|   |              |
|---|--------------|
| Spin inertia, $I_{A3}$ , kg-m <sup>2</sup> (slug-ft <sup>2</sup> ) . . . . .    | 14.36 (10.6) |
| Transverse inertia, $I_A$ , kg-m <sup>2</sup> (slug-ft <sup>2</sup> ) . . . . . | 7.18 (5.3)   |
| Mean radius of rim, $r_m$ , m (ft) . . . . .                                    | 0.8 (2.625)  |
| Mass of rim, $m_A$ , kg (slugs) . . . . .                                       | 22.48 (1.54) |

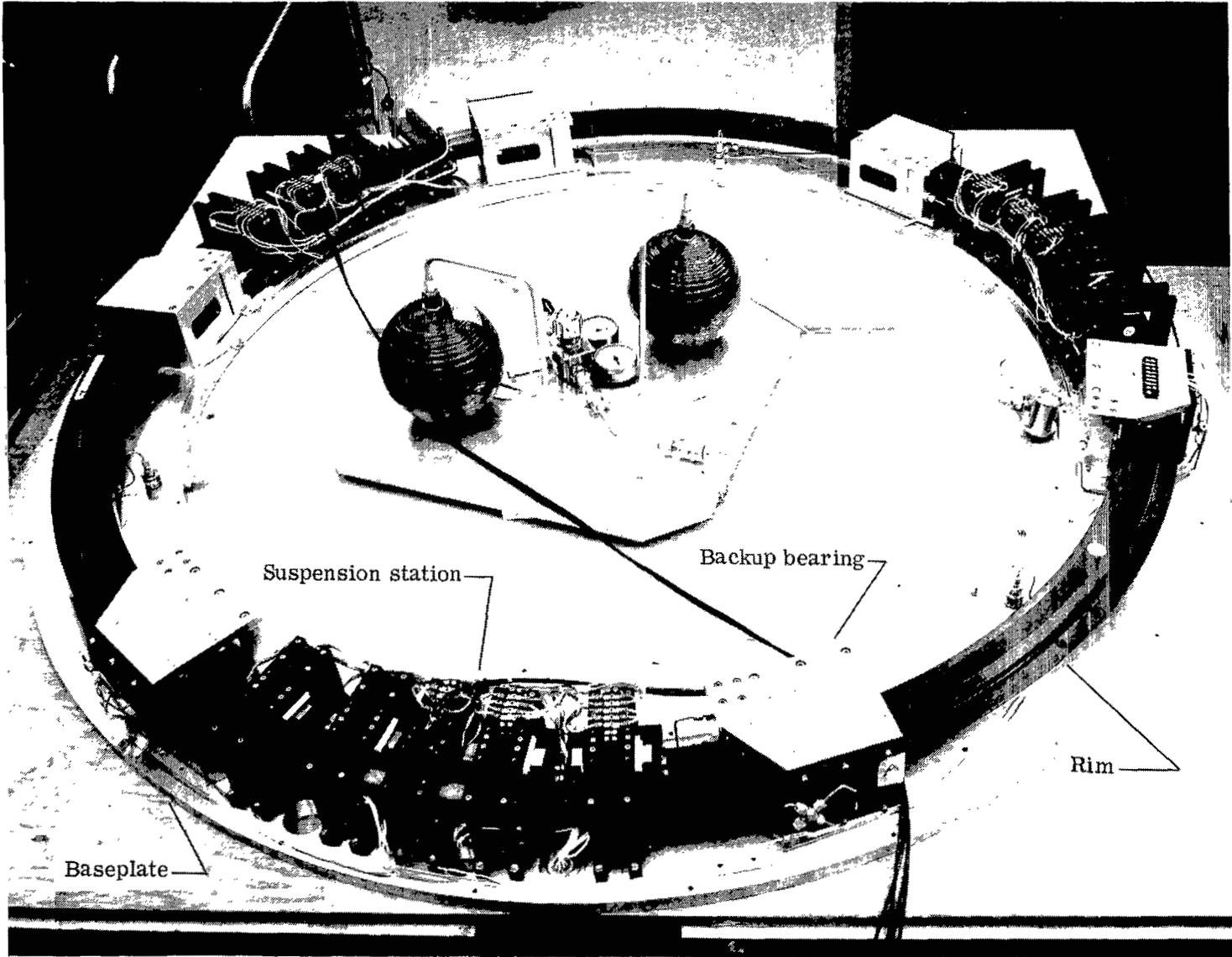


Figure A1.- AMCD laboratory model.

L-78-18.1

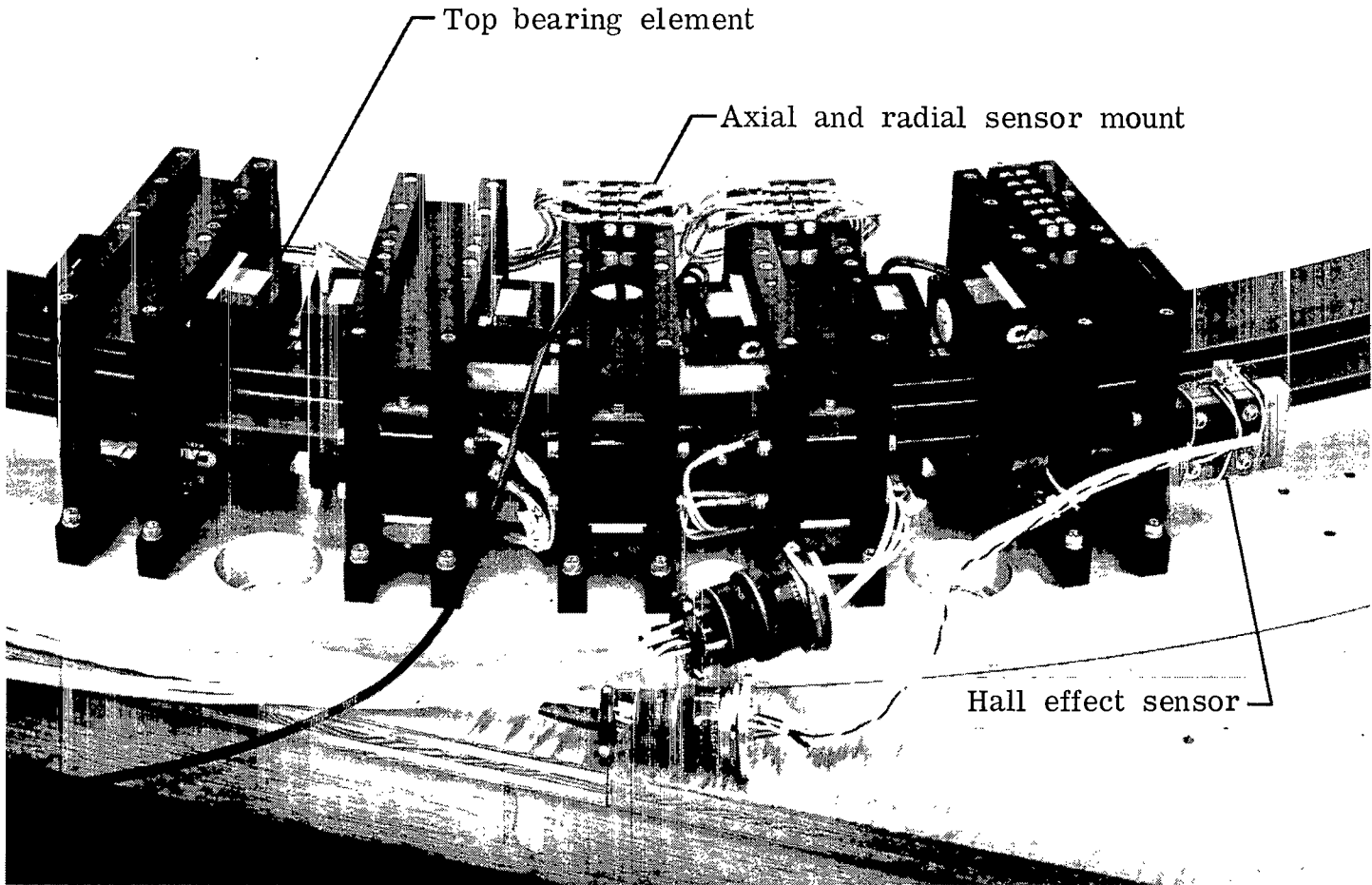
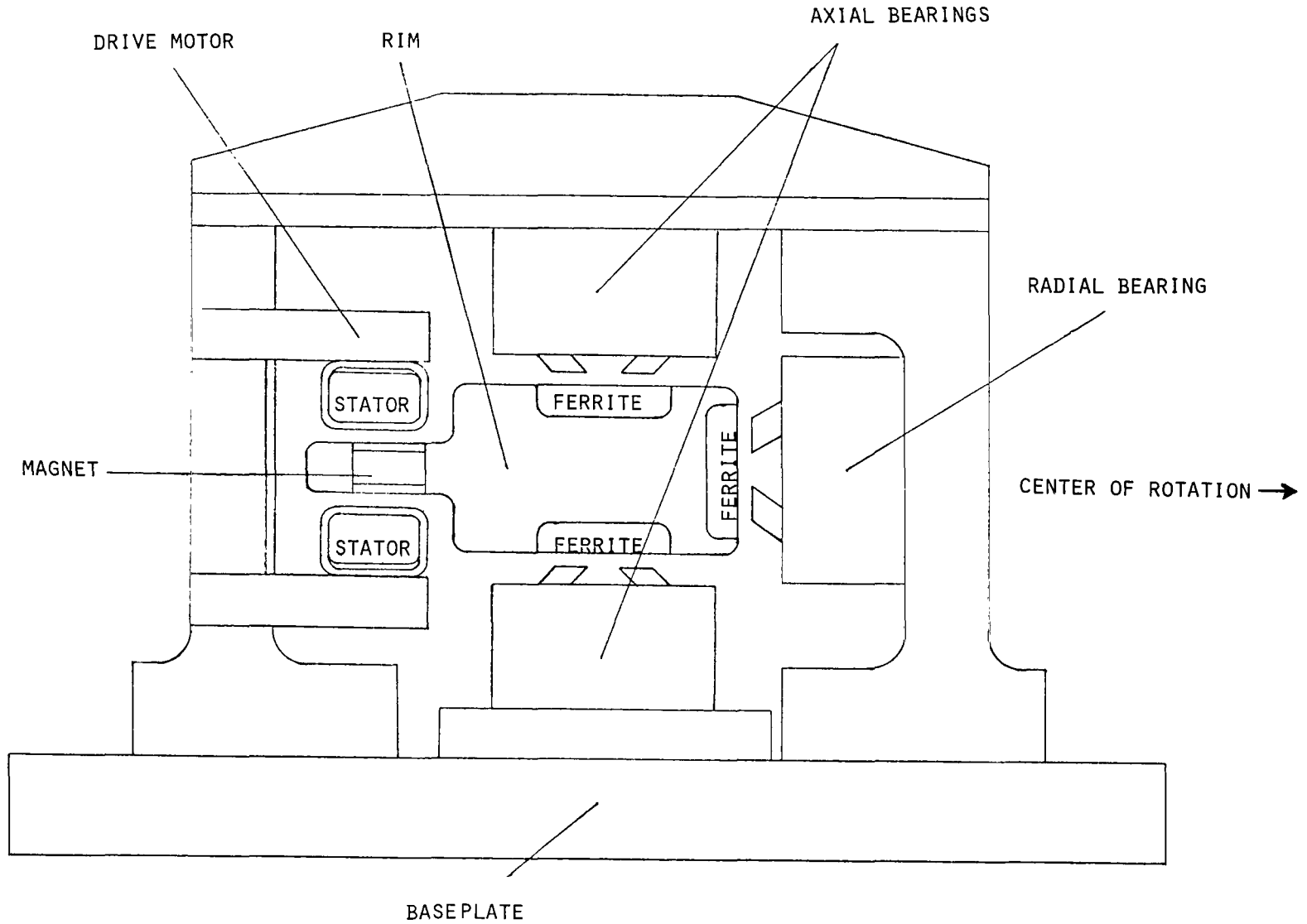


Figure A2.- AMCD suspension station.

L-78-19.1

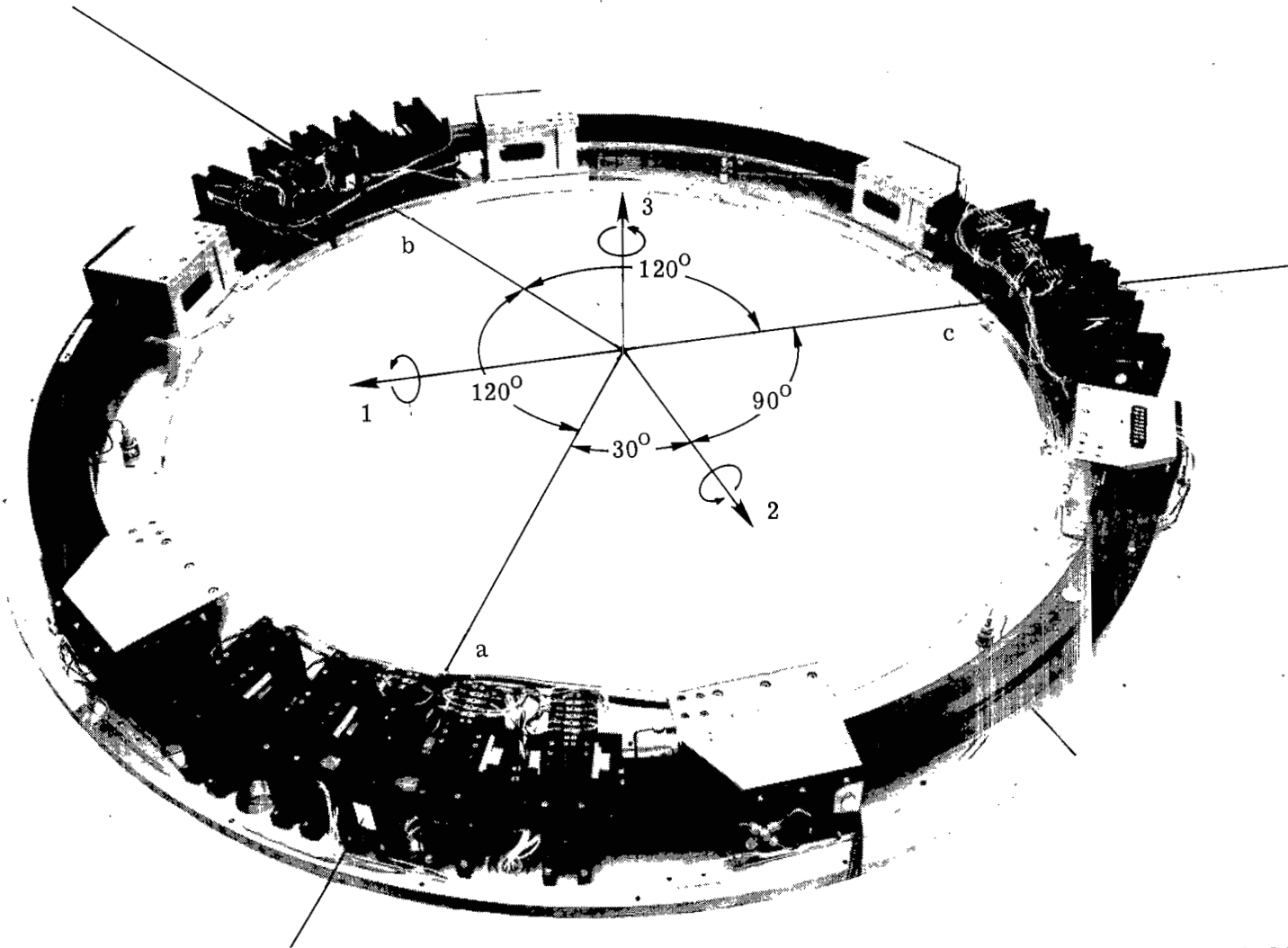


APPENDIX

Figure A3.- Cross-section drawing of an AMCD suspension station.

## REFERENCES

1. Anderson, Willard W.; and Groom, Nelson J.: The Annular Momentum Control Device (AMCD) and Potential Applications. NASA TN D-7866, 1975.
2. Schlieben, Ernest W.: Systems Aspects of Energy Wheels. Proceedings of the 1975 Flywheel Technology Symposium, G. C. Chang and R. G. Stone, eds., ERDA 76-85, Nov. 1975, pp. 40-52.
3. Aaland, Kristian; and Lane, Joe E.: Ideas and Experiments in Magnetic Interfacing. Proceedings of the 1975 Flywheel Technology Symposium, G. C. Chang and R. G. Stone, eds., ERDA 76-85, Nov. 1975, pp. 123-132.
4. Kirk, James A.; Studer, Philip, A.; and Evans, Harold E.: Mechanical Capacitor. NASA TN D-8185, 1976.
5. Ball Brothers Research Corp.: Annular Momentum Control Device (AMCD). Volume I: Laboratory Model Development. NASA CR-144917, [1976].
6. Groom, Nelson J.; and Terray, David E.: Evaluation of a Laboratory Test Model Annular Momentum Control Device. NASA TP-1142, 1978.
7. Woolley, Charles T.; and Groom, Nelson J.: Description of a Digital Computer Simulation of an Annular Momentum Control Device (AMCD) Laboratory Test Model. NASA TM-81797, 1981.
8. Groom, Nelson J.: Analytical Model of an Annular Momentum Control Device (AMCD) Laboratory Test Model Magnetic Bearing Actuator. NASA TM-80099, 1979.
9. Groom, Nelson J.: Fixed-Base and Two-Body Equations of Motion for an Annular Momentum Control Device (AMCD). NASA TM-78644, 1978.
10. Gupta, Someshwar C.; and Hasdorff, Lawrence: Fundamentals of Automatic Control. John Wiley & Sons, Inc., c.1970.



L-81-101

Figure 1.- Locations of magnetic bearing suspension stations a, b, and c with respect to AMCD axes 1, 2, and 3.

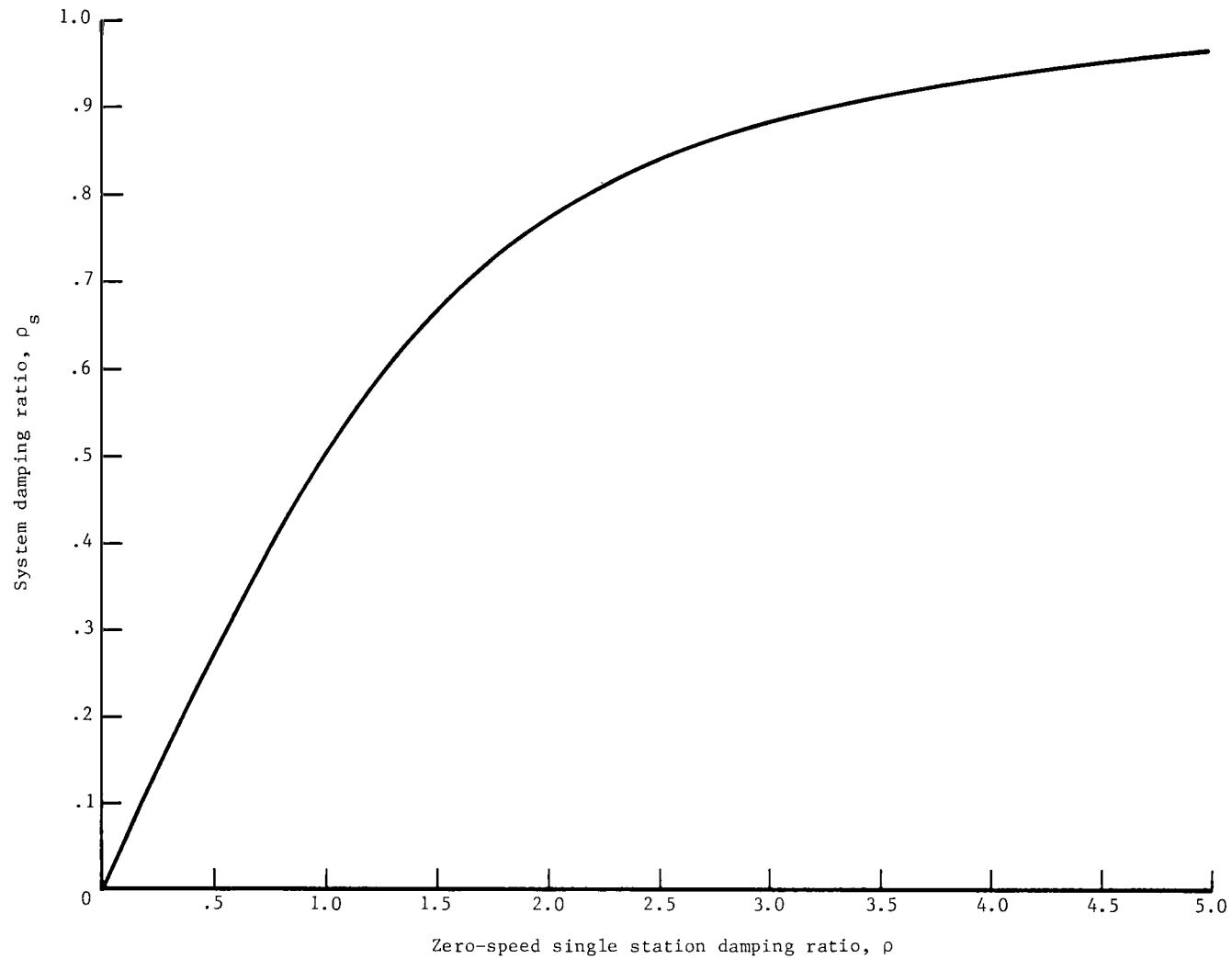


Figure 2.- System damping ratio at rated speed plotted against zero-speed single station damping ratio.

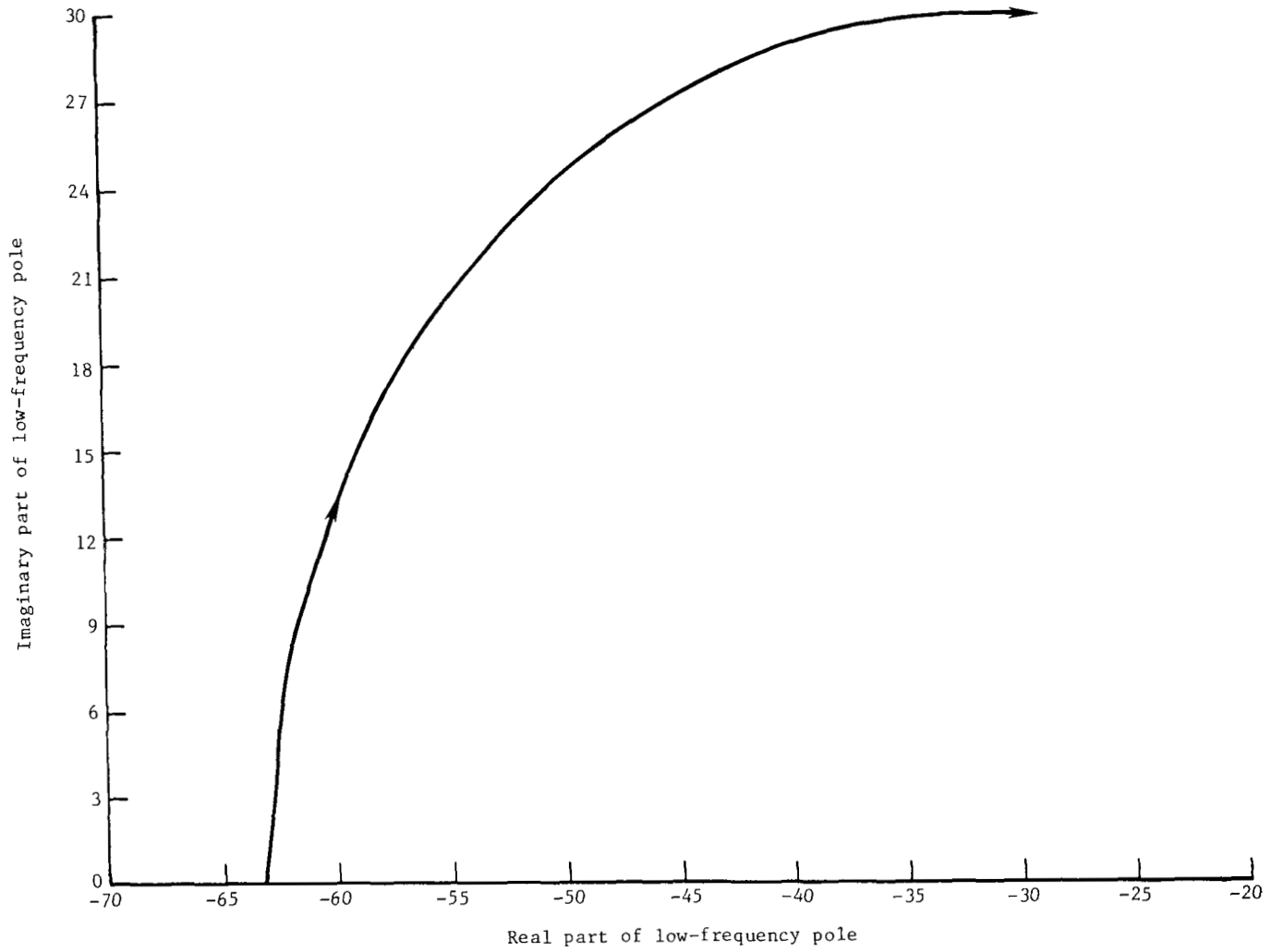


Figure 3.- Motion of low-frequency poles as rim speed varies from 0 to 2700 rpm.

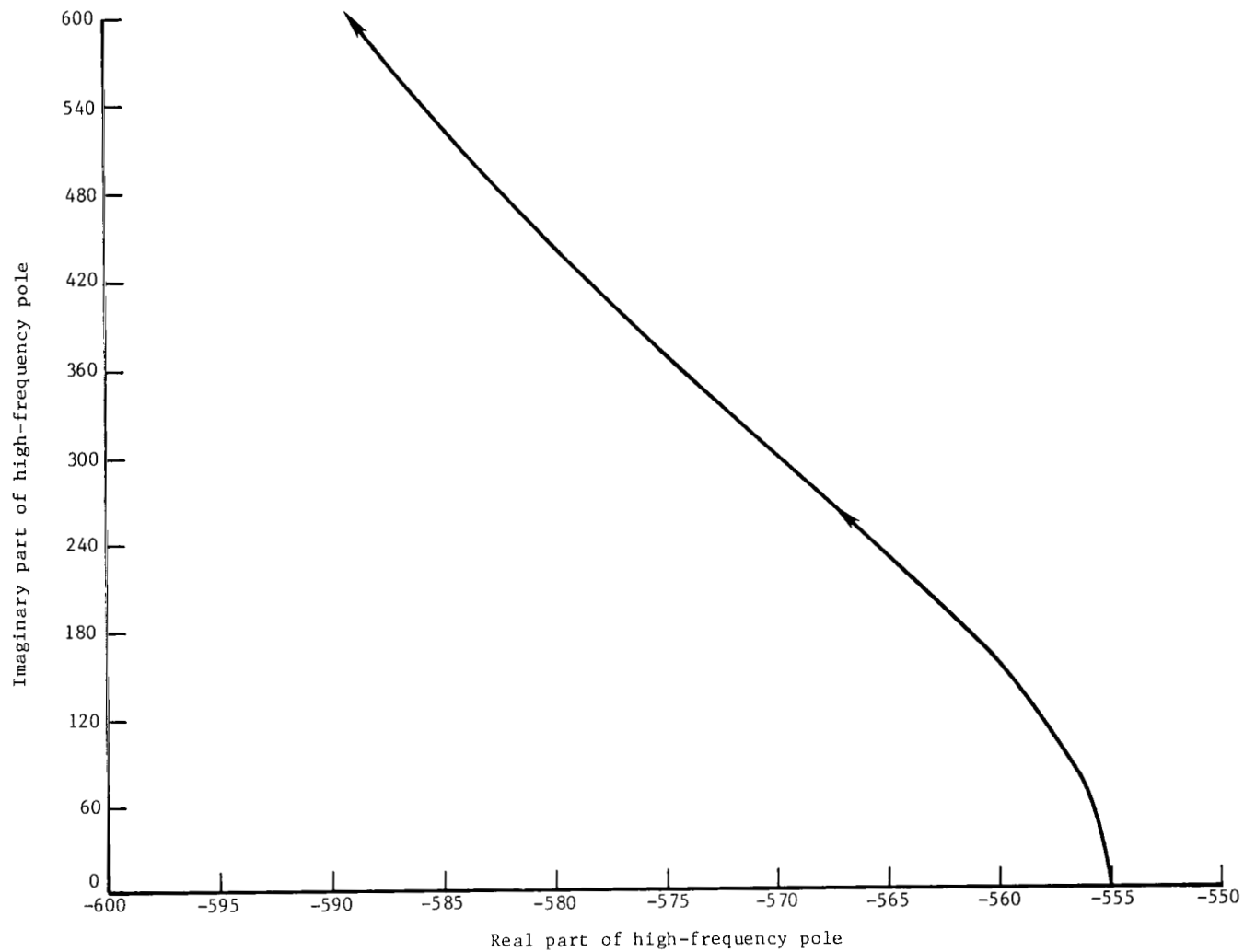


Figure 4.- Motion of high-frequency poles as rim speed varies from 0 to 2700 rpm.

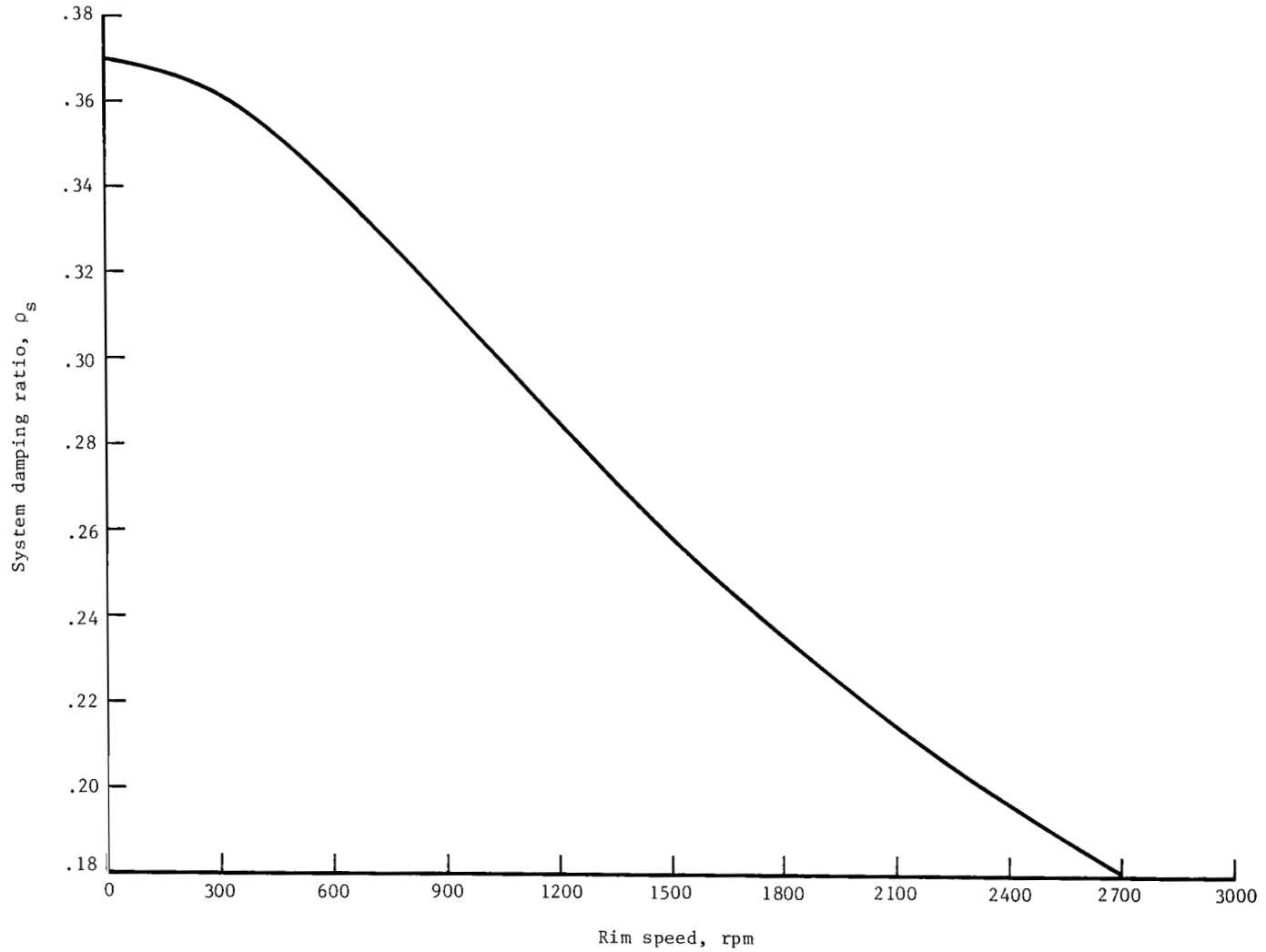


Figure 5.- Variation of system damping ratio with rim speed.

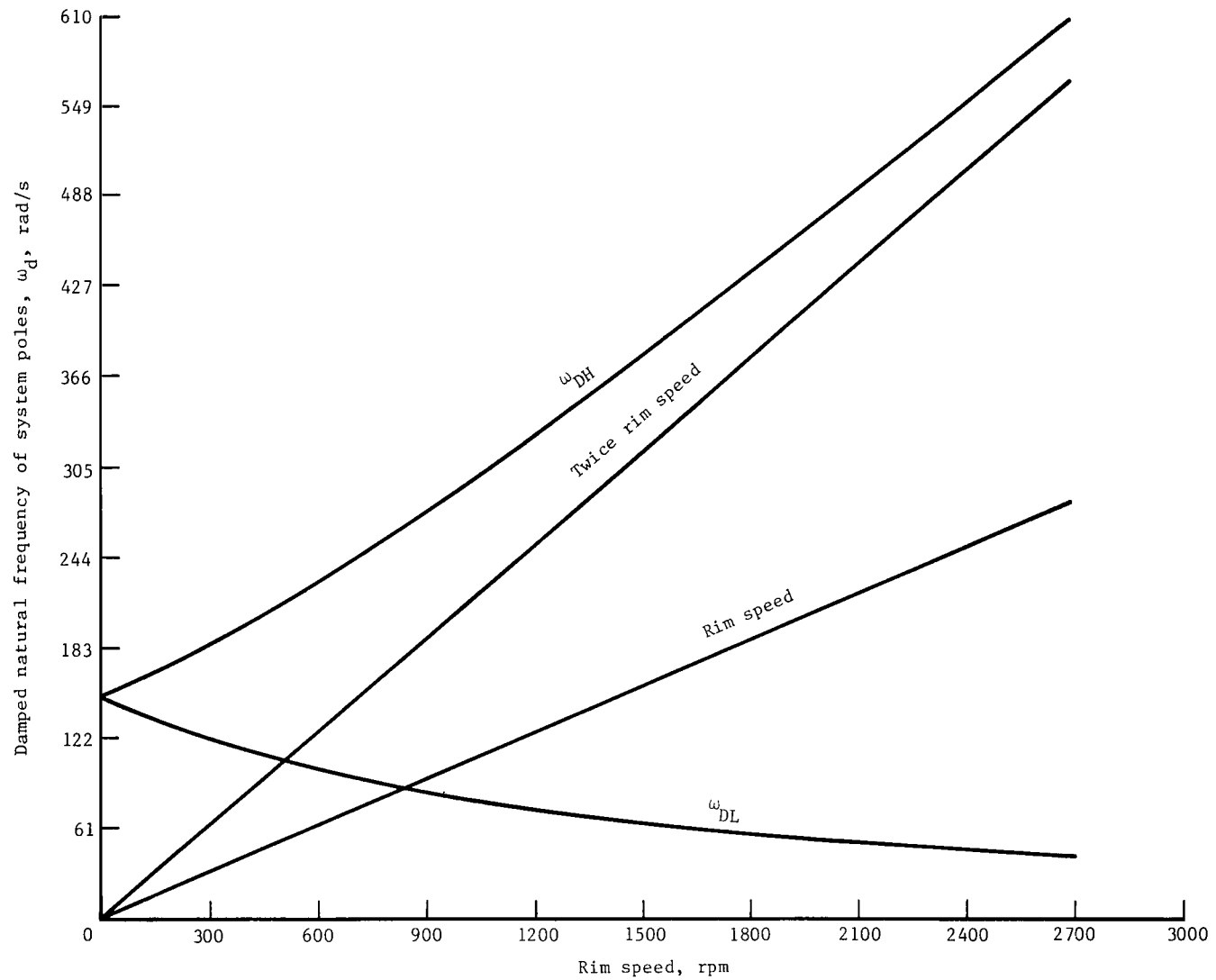


Figure 6.- Variation of damped natural frequency of system poles with rim speed.

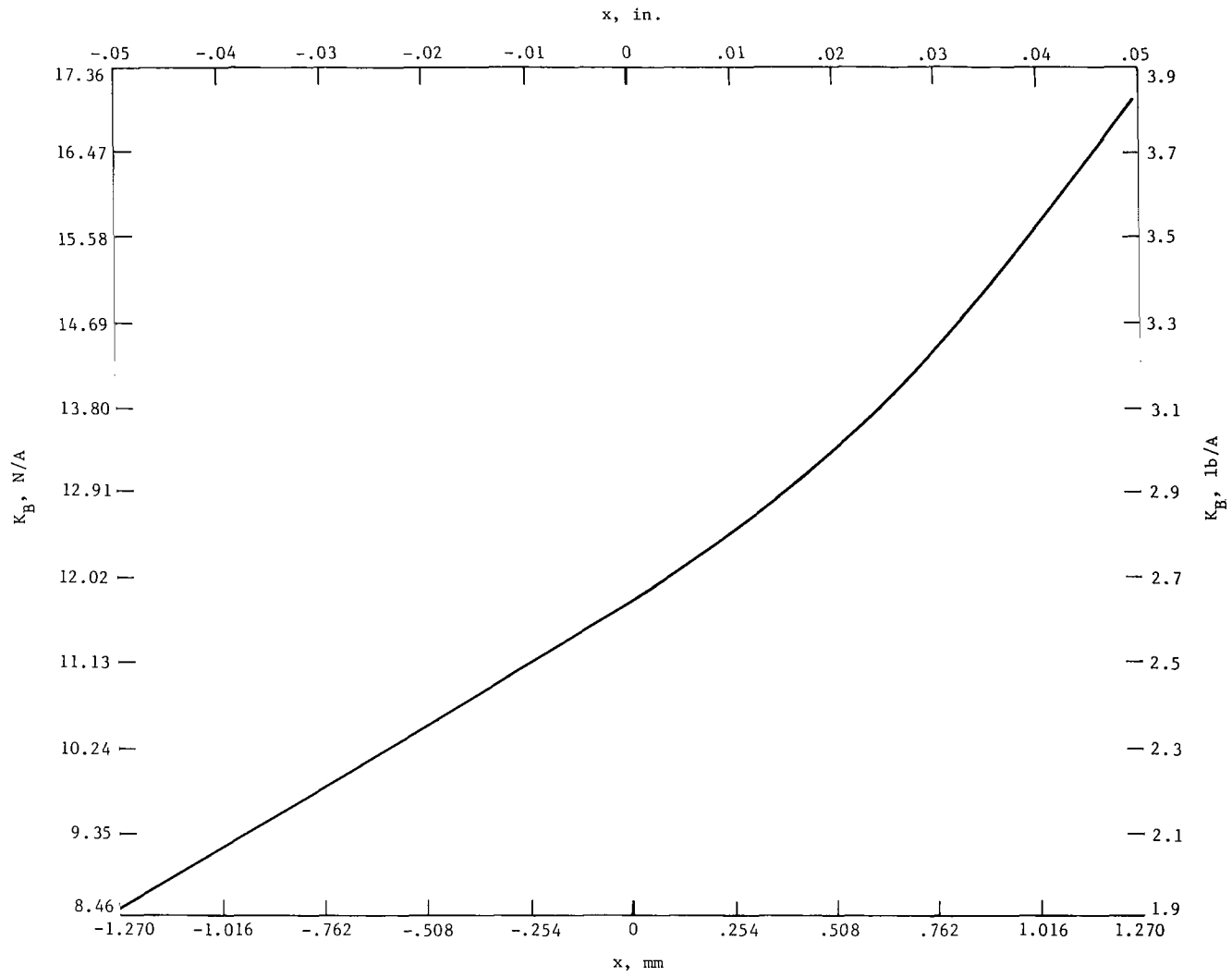


Figure 7.- Variation of  $K_B$  with nominal operating point  $x$  of rim in bearing gap.

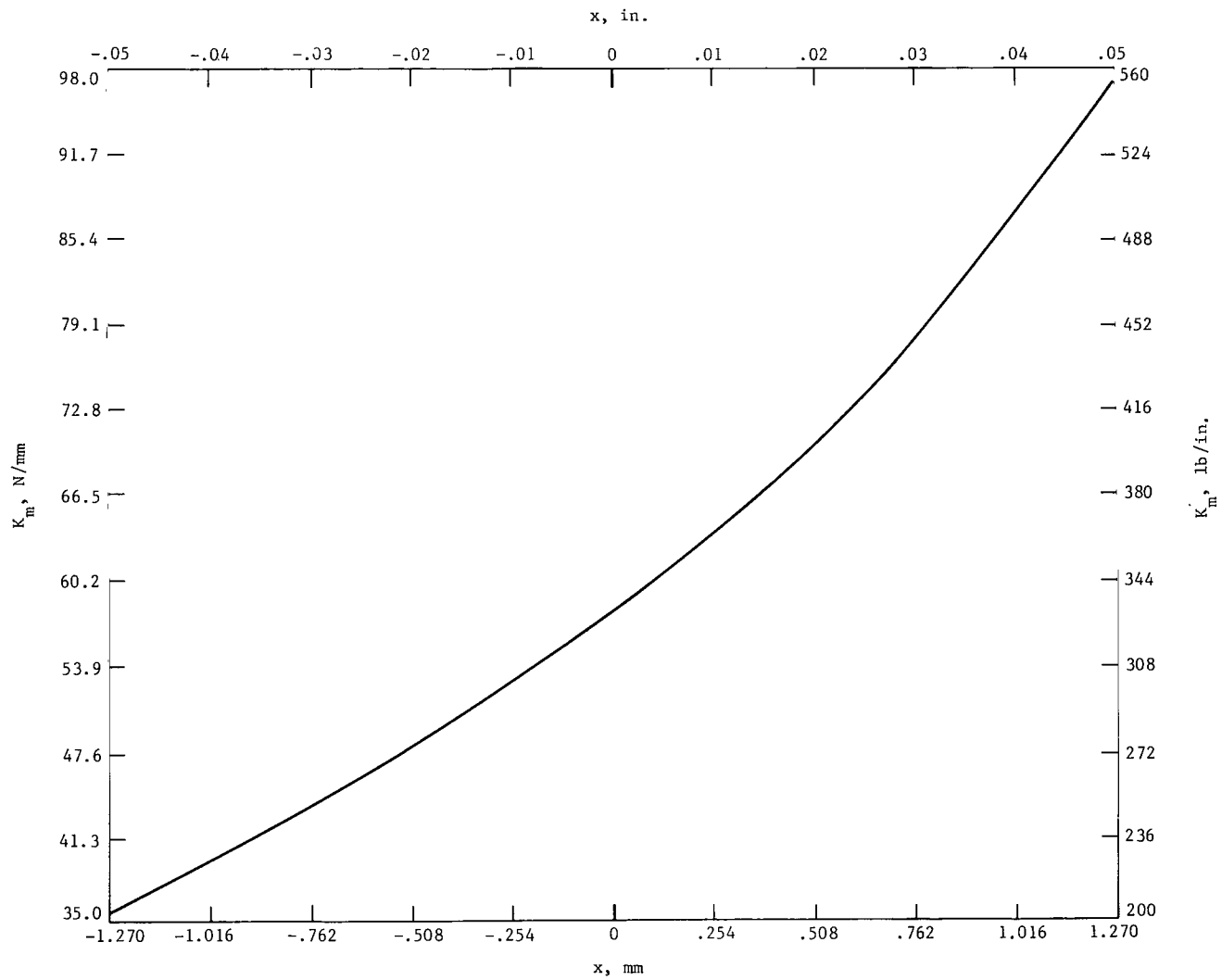


Figure 8.- Variation of  $K_m$  with nominal operating point  $x$  of rim in bearing gap.

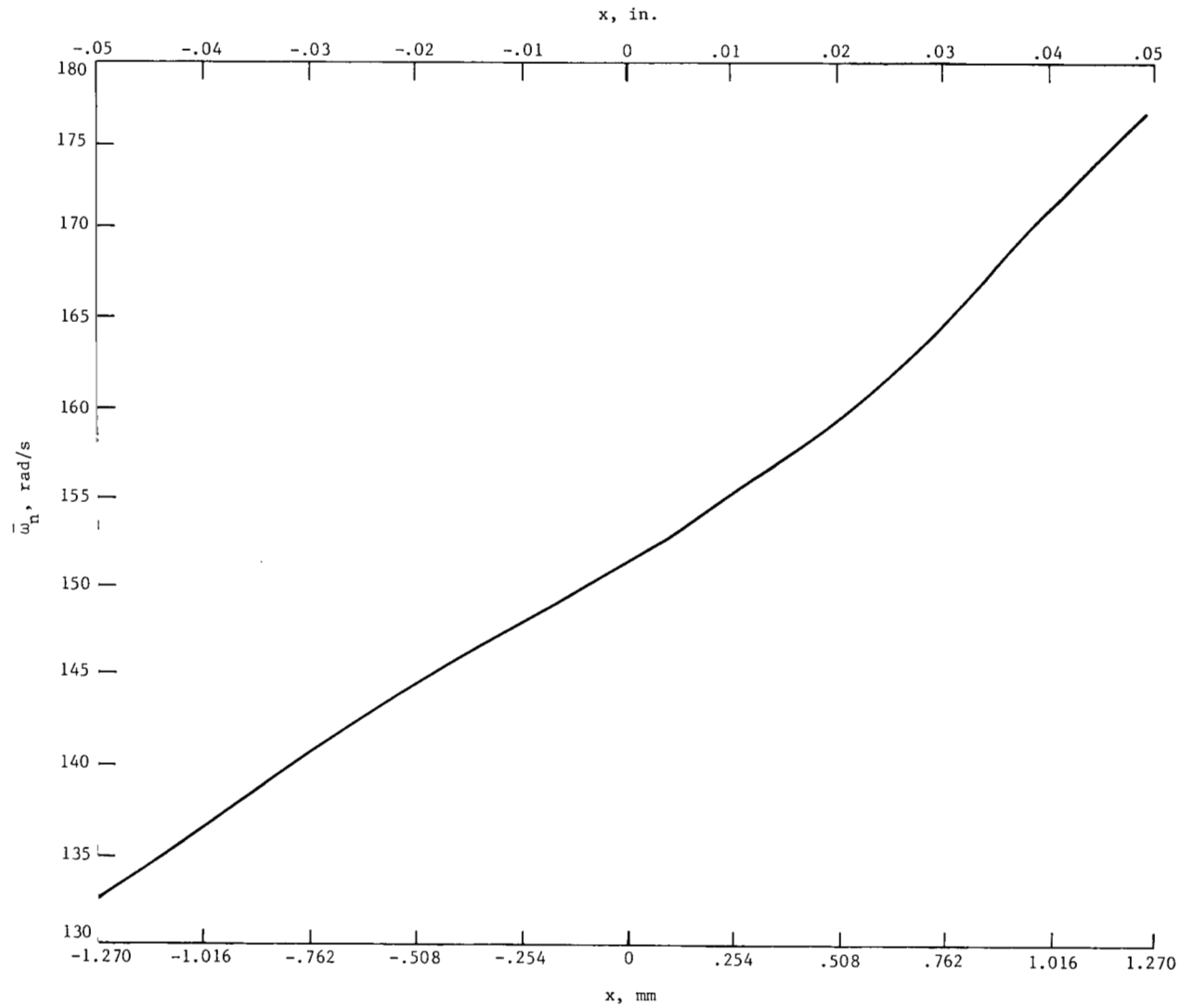


Figure 9.- Variation of  $\bar{\omega}_n$  with nominal operating point  $x$  of rim in bearing gap.

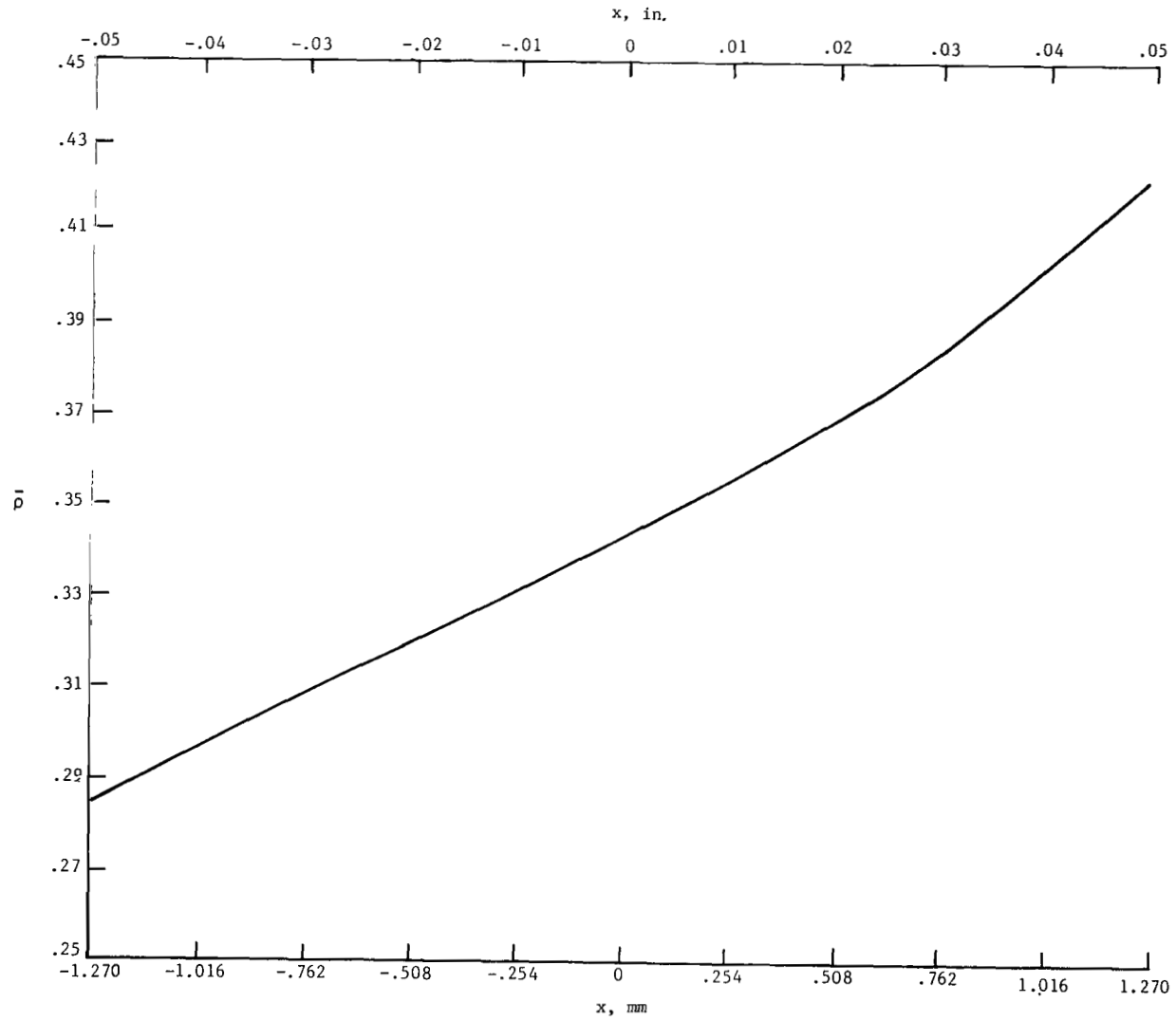


Figure 10.- Variation of  $\bar{p}$  with nominal operating point  $x$  of rim in bearing gap.

① Warp amplitude, 0.09525 mm (0.00375 in.)

② Warp amplitude, 0.1905 mm (0.0075 in.)

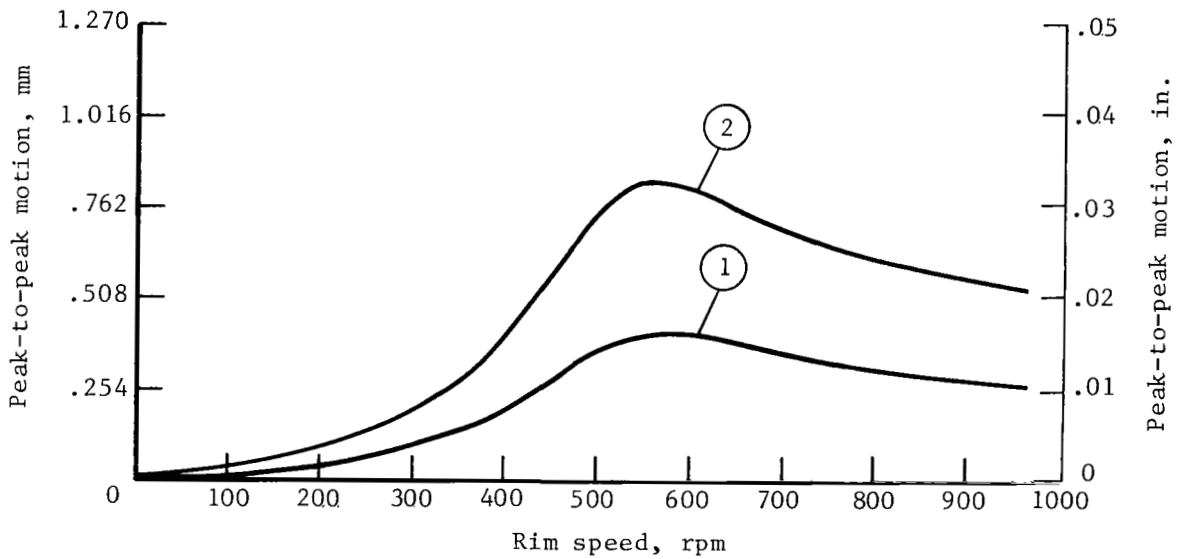
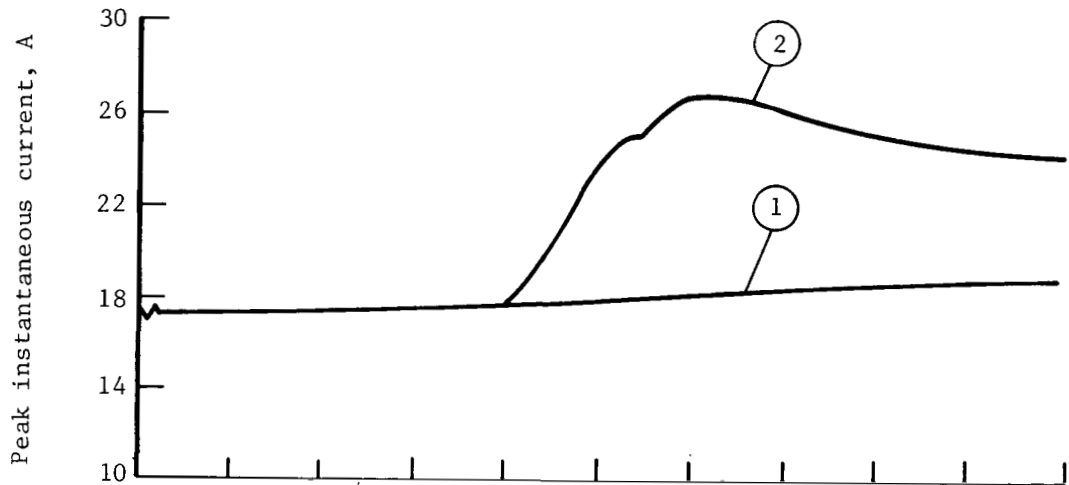


Figure 11.- Simulation results for nonlinear distributed magnetic bearings.

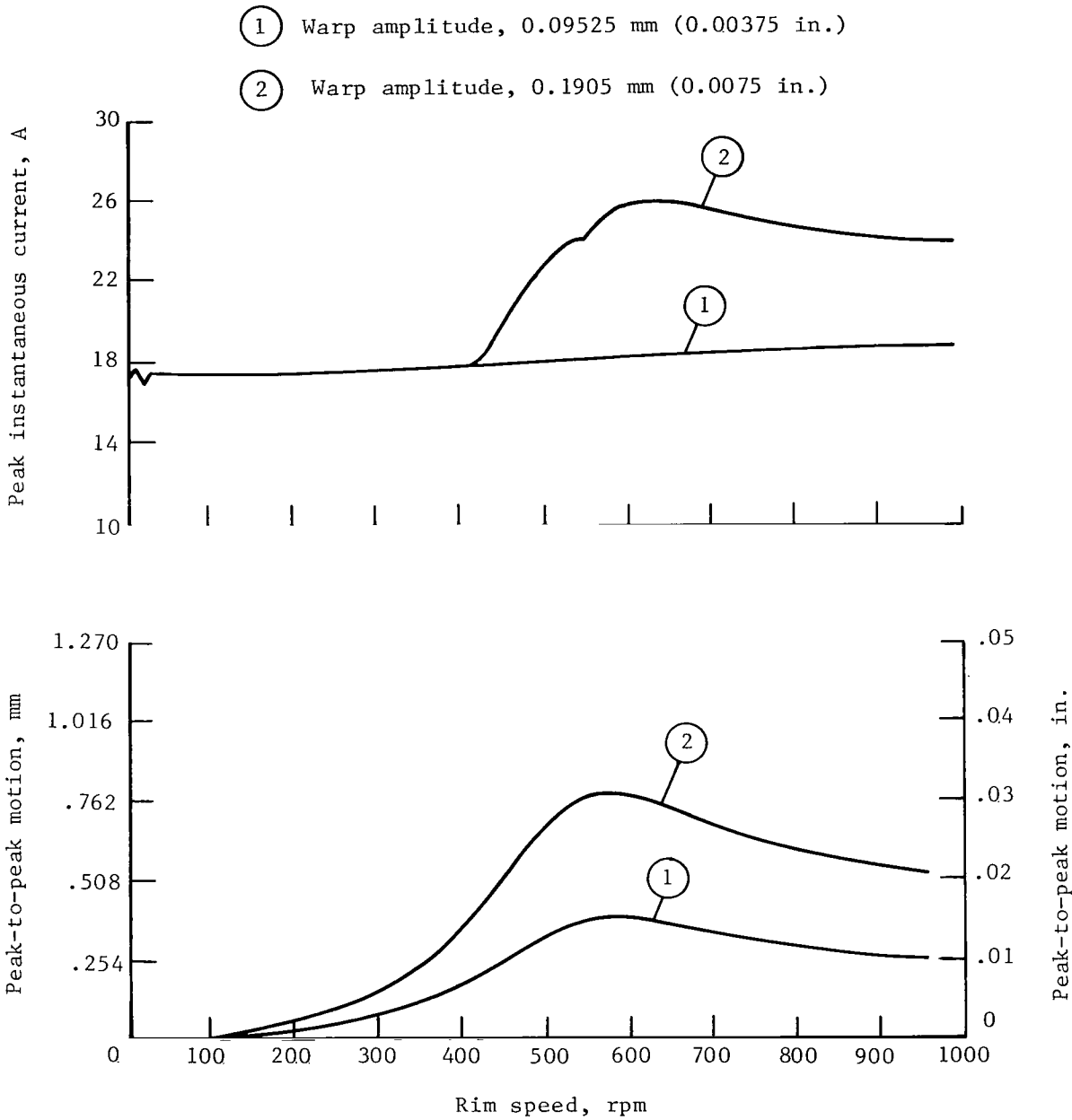


Figure 12.- Simulation results for nonlinear single point magnetic bearings.

- ① Warp amplitude, 0.09525 mm (0.00375 in.)
- ② Warp amplitude, 0.1905 mm (0.0075 in.)

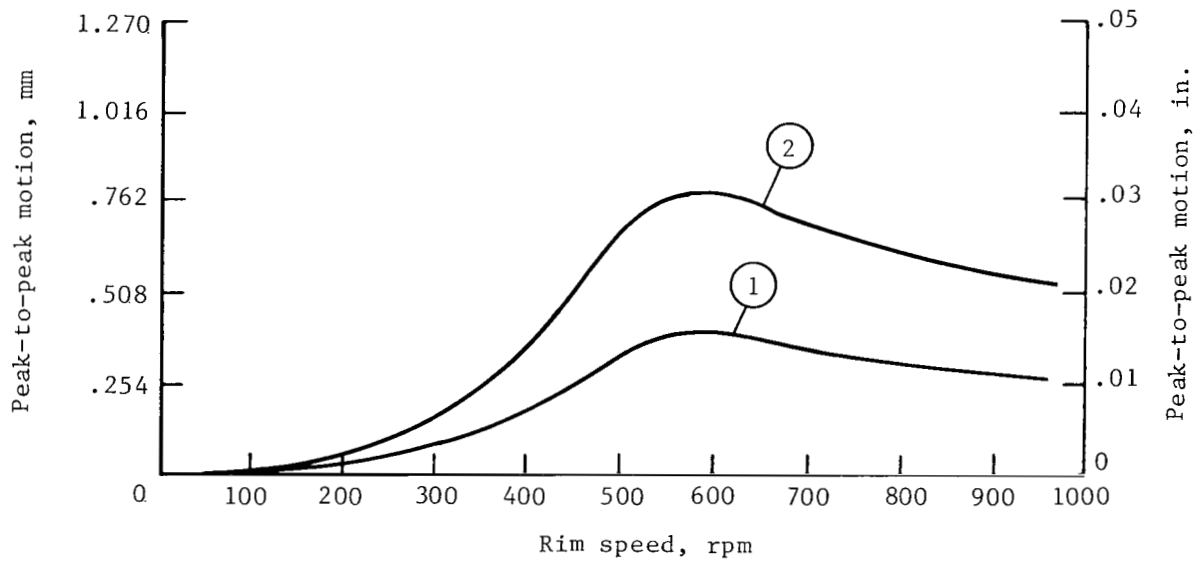
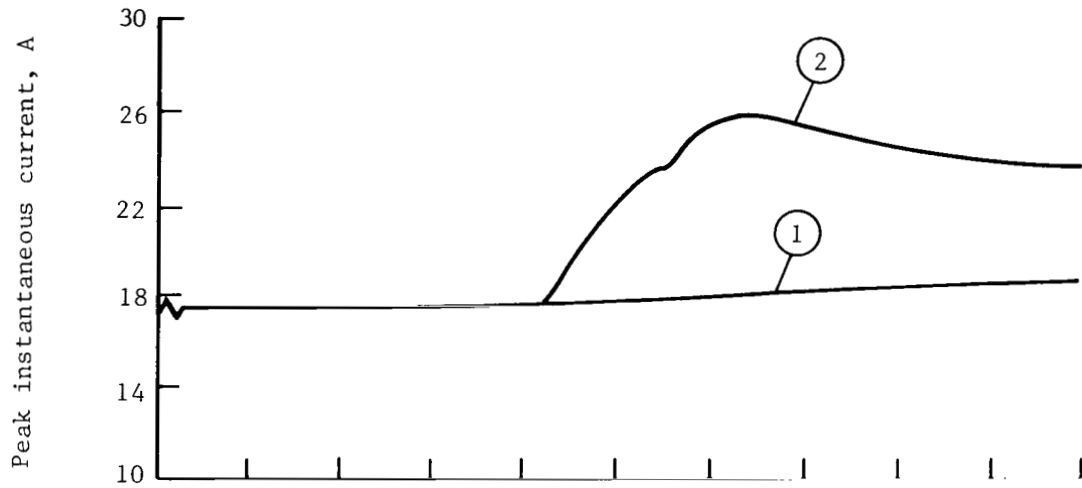


Figure 13.- Simulation results for linear single point magnetic bearings.

|   |  |                             |   |  |  |
|---|--|-----------------------------|---|--|--|
| 1. Report No.<br>NASA TP-1799   |  | 2. Government Accession No. |   | 3. Recipient's Catalog No.                               |  |
| 4. Title and Subtitle<br>ANALYSIS AND SIMULATION OF A MAGNETIC BEARING<br>SUSPENSION SYSTEM FOR A LABORATORY MODEL ANNULAR<br>MOMENTUM CONTROL DEVICE   |  |                             |   | 5. Report Date<br>March 1981                             |  |
|   |  |                             |   | 6. Performing Organization Code<br>506-54-93-02          |  |
| 7. Author(s)<br>Nelson J. Groom, Charles T. Woolley, and<br>Suresh M. Joshi   |  |                             |   | 8. Performing Organization Report No.<br>L-12403         |  |
|   |  |                             |   | 10. Work Unit No.  |  |
| 9. Performing Organization Name and Address<br>NASA Langley Research Center<br>Hampton, VA 23665  |  |                             |   | 11. Contract or Grant No.                                |  |
|   |  |                             |   | 13. Type of Report and Period Covered<br>Technical Paper |  |
| 12. Sponsoring Agency Name and Address<br>National Aeronautics and Space Administration<br>Washington, DC 20546   |  |                             |   | 14. Sponsoring Agency Code                               |  |
|   |  |                             |   |  |  |
| 15. Supplementary Notes<br>Nelson J. Groom and Charles T. Woolley: Langley Research Center<br>Suresh M. Joshi: Vigyan Research Associates, Inc., Hampton, Va.   |  |                             |   |  |  |
| 16. Abstract<br><br>A linear analysis and the results of a nonlinear simulation of a magnetic bearing suspension system which uses permanent magnet flux biasing are presented. The magnetic bearing suspension is part of a 4068 N-m-s (3000 lb-ft-sec) laboratory model annular momentum control device (AMCD). Included in the simulation are rigid body rim dynamics, linear and nonlinear axial actuators, linear radial actuators, axial and radial rim warp, and power supply and power driver current limits. |  |                             |   |  |  |
| 17. Key Words (Suggested by Author(s))<br>Spacecraft control actuator<br>Momentum storage device<br>Magnetic suspension   |  |                             | 18. Distribution Statement<br>Unclassified - Unlimited<br><br>Subject Category 31 |  |  |
| 19. Security Classif. (of this report)<br>Unclassified  | 20. Security Classif. (of this page)<br>Unclassified | 21. No. of Pages<br>36      | 22. Price<br>A03  |  |  |

For sale by the National Technical Information Service, Springfield, Virginia 22161

National Aeronautics and  
Space Administration

THIRD-CLASS BULK RATE

Postage and Fees Paid  
National Aeronautics and  
Space Administration  
NASA-451



Washington, D.C.  
20546

Official Business  
Penalty for Private Use, \$300

6 1 10, D, 030981 S00903DS  
DEPT OF THE AIR FORCE  
AF WEAPONS LABORATORY  
ATTN: TECHNICAL LIBRARY (SUL)  
KIRTLAND AFB NM 87117

**NASA**

POSTMASTER: If Undeliverable (Section 158  
Postal Manual) Do Not Return

---